



How mountain geometry affects aerosol-cloud-precipitation interactions: part II. Deep convective clouds

Jaemyeong Mango Seo¹ · Jong-Jin Baik¹

Received: 29 April 2025 / Accepted: 16 September 2025
© The Author(s) 2025

Abstract

The sensitivity of aerosol effects on orographic precipitation from deep convective clouds to mountain upslope steepness is examined using the Weather Research and Forecasting (WRF) model coupled with a bin microphysics scheme. During the early stage, the sensitivity resembles that of warm, shallow orographic convection as discussed in Part I. As time progresses, interactions between vigorously developed lower-layer clouds and upstream-extending upper-layer clouds become crucial for enhancing surface precipitation via melting and direct sedimentation of ice-phase particles such as graupel and hail. In the simulations with a symmetric mountain shape, higher aerosol number concentration enhances surface precipitation through stronger condensational latent heating and more active mixed-phase processes (freezing, Wegener-Bergeron-Findeisen process, and riming). Under asymmetric mountain shapes, however, the sensitivities are non-monotonic. In the steep upslope cases, fast liquid drop growth in the clean case and strong latent heating in the polluted case both support cloud development and enhance precipitation. In contrast, the control case produces less precipitation because its drop growth is slower than in the clean case and its latent heating is weaker than in the polluted case. As a result, cloud interaction is suppressed. In the gentle upslope cases, the control case shows the most precipitation due to sufficient droplet supply and latent heating which promote vertical growth and cloud interaction. The clean case lacks enough droplets, while the polluted case suffers from weak convection despite strong aerosol-induced heating. Consequently, both cases exhibit suppressed cloud interaction and mixed-phase processes.

Keywords Aerosol-cloud-precipitation interactions · Aerosol number concentration · Mountain upslope geometry · Orographic precipitation · Bin microphysics

1 Introduction

Aerosol loading controls precipitation characteristics through complex aerosol-cloud-precipitation interactions, because aerosol particles act as cloud condensation nuclei (CCN) or ice nuclei (IN) in the atmosphere. To understand the role of aerosol particles in controlling precipitation characteristics, many researchers have investigated the impacts of aerosols on clouds and precipitation extensively (e.g., Khain 2009; Tao et al. 2012; Fan et al. 2016). These aerosol effects can become particularly complex in mountainous regions.

Precipitation over mountainous regions, known as orographic precipitation, is affected by various factors, including mountain geometry as well as background static stability, wind speed, and humidity (Colle 2004; Pathirana et al. 2005; Roe and Baker 2006). However, the sensitivity of orographic precipitation to the environmental factors and mountain geometry is generally focused on orographic precipitation from shallow clouds, because in a broad range of the environmental factors and mountain geometry, subsidence aloft on the windward side can limit convective development of orographic clouds. Several studies have investigated orographic precipitation in the conditionally unstable atmosphere and have categorized the behavior of convective orographic clouds depending on convective available potential energy (CAPE), mountain width, and the Froude number ($F = U/Nh_m$), where U is the background wind speed, N is the background buoyancy frequency, and h_m is the maximum height of the mountain

✉ Jaemyeong Mango Seo
mangoseo@snu.ac.kr

¹ School of Earth and Environmental Sciences, Seoul National University, Seoul 08826, South Korea

(e.g., Chu and Lin 2000; Chen and Lin 2005; Chen et al. 2008; Miglietta and Rotunno 2009; Sever and Lin 2017).

Many previous studies have shown that the increase in aerosol number concentration usually results in decrease in surface precipitation from shallow convection (Xue and Feingold 2006; Cheng et al. 2007; Fan et al. 2012) and in increase in surface precipitation from deep convection (Khain et al. 2005; Rosenfeld et al. 2008; Clavner et al. 2018). Recent studies have further refined this understanding by highlighting the dominant role of CCN in glaciation (Munawar et al. 2025) and the contrasting effects of different aerosol types on cloud microphysics (Chen et al. 2025).

In orographic convection, aerosol-cloud-precipitation interactions exhibit greater complexity due to terrain-modulated airflow and microphysical variability. Many studies have shown that air pollution causes suppression of orographic precipitation (Givati and Rosenfeld 2004; Jirak and Cotton 2006; Rosenfeld and Givati 2006; Rosenfeld et al. 2007; Guo et al. 2014). Xiao et al. (2015) showed that the increase in aerosol number concentration results in the enhanced orographic precipitation, but the effects on deep convective orographic precipitation have been less studied. The recent work by Chavez and Barros (2023) further indicates that aerosol indirect effects can shift the spatial distribution of orographic precipitation, especially by modifying cloud lifetime and riming processes along windward slopes.

Bin microphysics models predict the evolution of each size bin of each hydrometeor separately, allowing detailed tracking of microphysical growth and phase changes (e.g., Khain et al. 2000; Lynn et al. 2005a, b). To investigate the microphysical processes under orographic precipitation more precisely, numerical studies using bin microphysics schemes have been conducted (Lynn et al. 2007; Xue et al. 2010; Xiao et al. 2014). However, most of these studies have focused on shallow convective orographic clouds, where warm rain processes dominate. Relatively few studies have used bin schemes to examine deep orographic convection involving mixed-phase microphysics; Xiao et al. (2015), for example, investigated aerosol effects on mixed-phase orographic precipitation, but such work remains limited.

This study is an extension of Seo et al. (2020; hereafter Part I) which investigated how windward slope geometry influences aerosol-cloud-precipitation interactions in shallow orographic convection using a bin microphysics model. To isolate the effects of upslope-driven processes, only the windward slope was varied while the leeward slope was held constant. Part I showed that increasing aerosol number concentration leads to a reduction in precipitation and a downwind shift of precipitation, with these effects being most pronounced for steeper windward slope. These findings suggest that upslope geometry plays a crucial role in modulating aerosol-cloud-precipitation interactions. However, the

analysis in Part I was limited to warm clouds without ice-phase processes.

In this study, we extend our investigation to deep mixed-phase orographic convection, in which clouds develop above the freezing level and additional microphysical processes, together with mountain-induced airflow, may affect how upslope geometry modulates aerosol-cloud-precipitation interactions. Section 2 describes the experimental design of the simulations. Sections 3.1 and 3.2 present the characteristics of deep convective orographic precipitation and its sensitivity to aerosol number concentration. Section 3.3 discusses how aerosol effects vary with changes in the windward mountain slope. Section 4 provides a summary and concluding remarks.

2 Simulation design

In this study, the Weather Research and Forecasting (WRF) model (Skamarock et al. 2008), version 3.6.1, coupled with the Hebrew University Cloud Model (HUCM) (Khain and Sednev 1996; Khain et al. 2004) is used (Lee and Baik 2016). The model is the same as in Part I, except that mixed-phase microphysical processes are included. This model predicts seven types of hydrometeors [liquid drops, ice crystals (column, plate, and dendrite), snow, graupel, and hail] as well as aerosols, which are subdivided into 43 mass-doubling bins. Detailed descriptions of HUCM are provided in Khain et al. (2000, 2004, 2011), and additional details on the treatment of aerosols in the WRF-bin model can be found in Lee and Baik (2016).

Two-dimensional simulations are conducted to examine orographic precipitation from deep convective clouds. Figure 1 shows the schematic of the simulations. The bell-shaped mountain, defined as below, triggers orographic clouds by forced uplift.

$$h(x) = h_m \frac{a^2}{x^2 + a^2}. \quad (1)$$

Here, $h_m = 2$ km is the maximum height and a ($= a_1$ for $x < 0$ km and $= a_2 = 10$ km for $x \geq 0$ km) is the half-width of the bell-shaped mountain. As in Part I, we classify simulation cases by aerosol number concentration at 1% supersaturation N_0 at the initial time [$= 100 \text{ cm}^{-3}$ in CLN (clean), $= 500 \text{ cm}^{-3}$ in CNT (control), and $= 2500 \text{ cm}^{-3}$ in PLT (polluted)] and the windward width (upslope steepness) of the mountain a_1 ($= 5$ km for narrow, $= 10$ km for control, and $= 20$ km for wide). Table 1 provides the name and specific settings for each case. The background wind speed $U = 10 \text{ m s}^{-1}$ is constant in the vertical.

Fig. 1 Schematic of the simulations. The dashed, solid, and dotted upslope shapes represent the mountains with narrow windward-width (steep upslope), symmetric width, and wide windward-width (gentle upslope), respectively. Tropopause is located at $z=12$ km, and the sponge layer is located from $z=15$ to 20 km. The vertical profiles of temperature T , dew point temperature (T_d), and relative humidity (H) are schematically illustrated

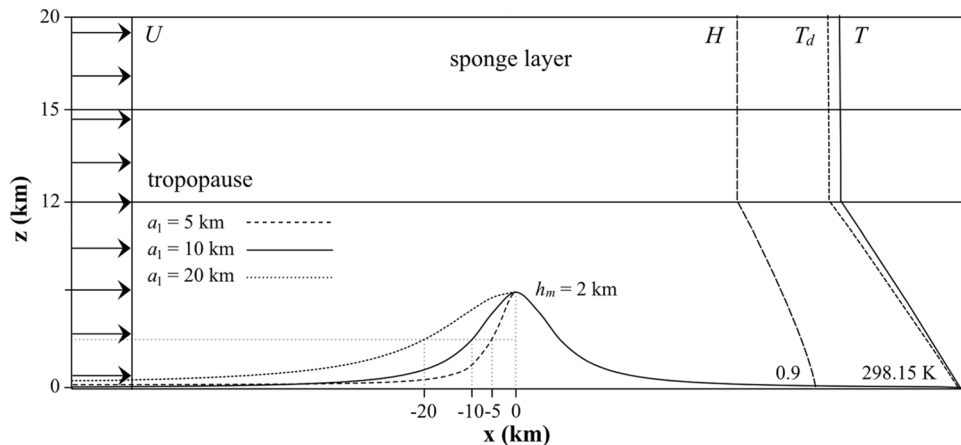


Table 1 Names of the nine simulation cases and the corresponding aerosol number concentrations (N_0) and windward half-widths (a_1) of the mountain

	N_0 (cm^{-3})	a_1 (km)
CLN	100	10
CNT	500	10
PLT	2500	10
CLNn	100	5
CNTn	500	5
PLTn	2500	5
CLNw	100	20
CNTw	500	20
PLTw	2500	20

To generate vigorous convective orographic clouds, a modified version of Weisman and Klemp (1982) sounding is used. In this study, the potential temperature θ and relative humidity H are given as follows:

$$\theta(z) = \begin{cases} \theta_0 \left(1 + \frac{N^2 z}{g} \right) & \text{for } z \leq z_{tr}, \\ \theta_{tr} \exp \left[\frac{g}{c_p T_{tr}} (z - z_{tr}) \right] & \text{for } z > z_{tr}. \end{cases} \quad (2)$$

$$H(z) = \begin{cases} H_0 \left[1 - \frac{3}{4} \left(\frac{z}{z_{tr}} \right)^{5/4} \right] & \text{for } z \leq z_{tr}, \\ H_{tr} & \text{for } z > z_{tr}, \end{cases} \quad (3)$$

where $\theta_0 = 298.15$ K and θ_{tr} [$H_0 (=0.9)$ and H_{tr}] are the potential temperature (relative humidity) at the surface and the tropopause height $z_{tr} (=12$ km), respectively. T_{tr} is the temperature at the tropopause, c_p is the specific heat of air at constant pressure, $N (=0.01 \text{ s}^{-1})$ is the buoyancy frequency, and g is the gravitational acceleration. By fixing N , the initial Froude number ($F=0.5$) is easily controlled. The skew $T\text{-log } p$ diagram of this sounding is shown in Fig. 2. The lifting condensation level (LCL ~ 300 m) is located below

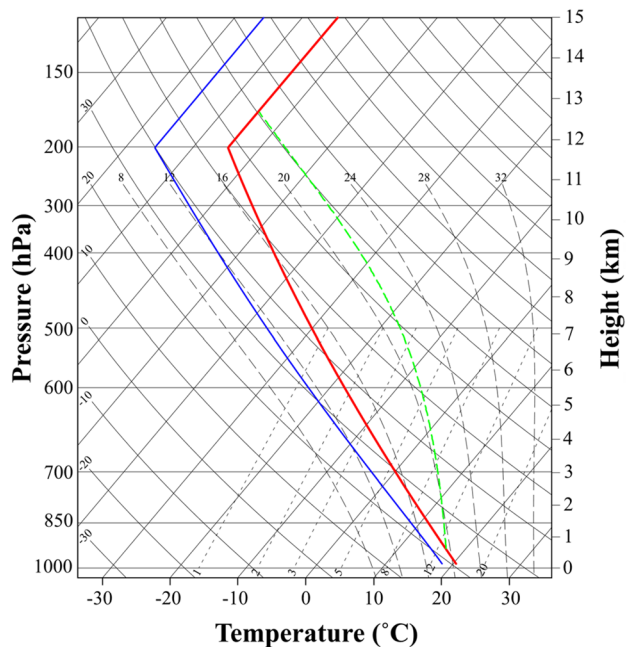


Fig. 2 Skew $T\text{-log } p$ diagram used in the nine simulations. This sounding is a modified version of the sounding in Weisman and Klemp (1982). The red, blue, and green lines represent the temperature, dew point temperature, and the moist adiabatic ascent from the level of free convection (LFC) to the equilibrium level (EL), respectively

the mountain top, which enables orographic cloud formation through forced uplift. Although the background atmosphere is statically stable ($N=0.01 \text{ s}^{-1}$), the sounding becomes highly unstable after saturation, with CAPE reaching 4457 J kg^{-1} . This allows deep and strong convection to develop through the tropopause.

A horizontal domain of 200 km with a horizontal grid size of 250 m is used. The vertical domain size is 20 km with a 5-km sponge layer and 401 terrain-following levels. The vertical grid spacing is approximately 50 m near the surface and increases with height. An open lateral boundary

condition is applied in the horizontal. Each case is integrated for 12 h using the WRF-bin model with a time step of 0.6 s. However, only the first 6 h of results are analyzed, for reasons discussed in Sect. 3.1. Except for the bin microphysics scheme and basic turbulent/diffusion parameterization, other parameterizations are not used.

3 Results and discussion

3.1 General characteristics of the simulated orographic precipitation

Figure 3 shows the mixing ratios of liquid drops (bluish shading), low-density ice particles (brownish shading), such as ice crystals and snow, and high-density ice particles (black contours), such as graupel and hail, along with wind vectors in the CNT case. From the early stage, orographic clouds are generated over the upslope. In the subcritical condition ($F < 1$), flows converge into a thin layer and accelerate over the downslope. As a result, a hydraulic jump occurs, and strong updrafts are generated over the downslope

(~ 10 km in Fig. 3a). Although the simulated wind field in this stage exhibits general subsidence over the windward slope, it does not yet resemble the canonical mountain wave structure described in classical theories (e.g., Smith 1979; Durran 1990). This discrepancy is likely due to early transient convective activity near the mountain.

The deep convective system is advected downstream by downslope wind and results in heavy precipitation on the lee of the mountain (~ 30 km in Fig. 3b). As the transiently generated deep convective system moves out of the depicted region, the simulated wind field gradually organizes into a more structured wave pattern, with alternating updrafts and downdrafts typical of stratified flow over topography. Following this transition, two vertically separated cloud layers become apparent (Fig. 3c).

The lower layer consists mainly of orographic clouds with liquid drops, while the upper layer is dominated by low-density ice particles. In the stratified atmosphere, the vertical growth of shallow orographic clouds is suppressed by persistent downdrafts in the lower layer. These downdrafts are induced both by the mountain wave and by flow convergence and acceleration along the downslope under subcritical

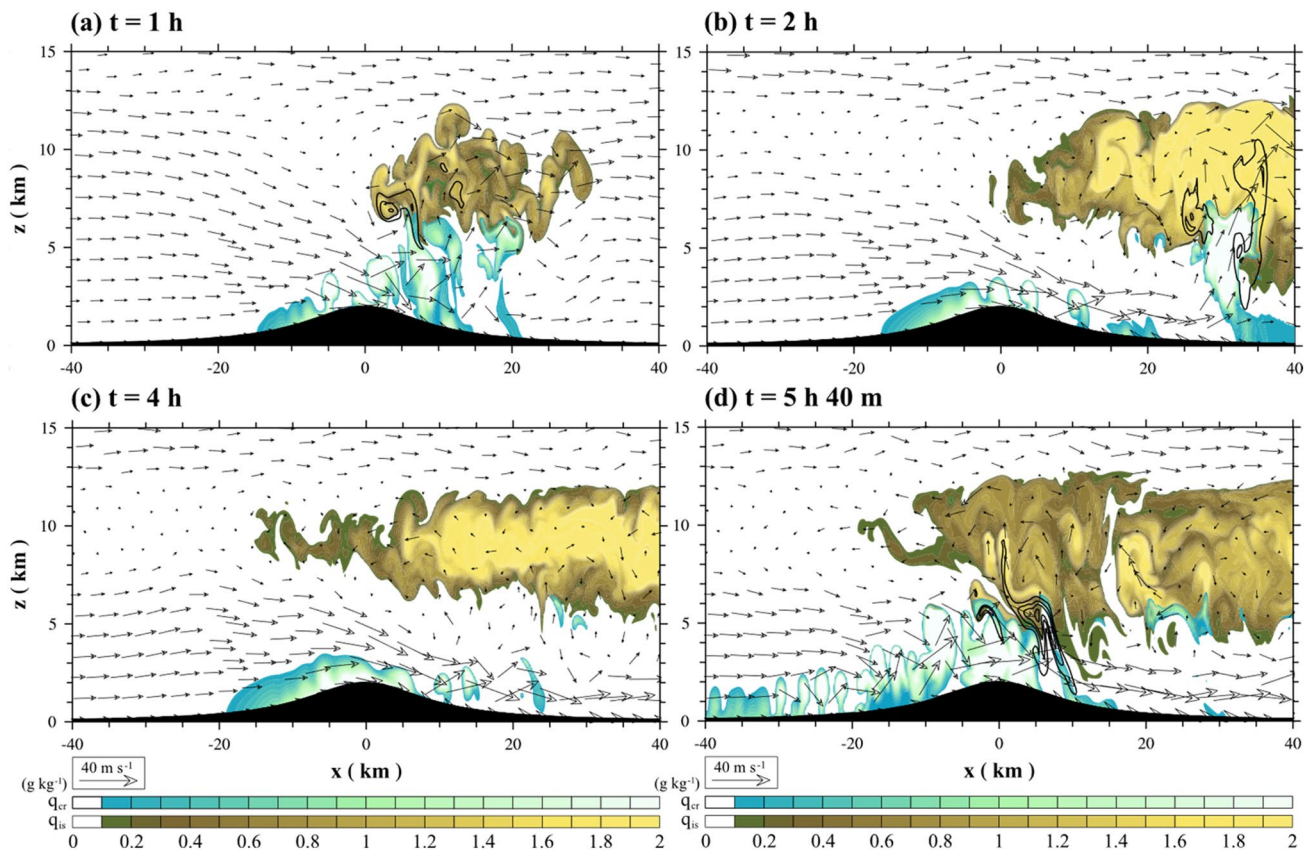


Fig. 3 Fields of mixing ratios of liquid drops (bluish shading), low-density ice particles (brownish shading), such as ice crystals and snow, and high-density ice particles (black contours), such as graupel

and hail, along with wind vectors at $t =$ (a) 1 h, (b) 2 h, (c) 4 h, and (d) 5 h 40 m in CNT. The contour interval of high-density ice particle mixing ratio is 0.02 g kg^{-1}

condition. In the upper layer over the lee side, particularly between 8 and 11 km altitude, weak updrafts generated by the wave structure facilitate the growth of pre-existing ice crystals into snow particles. Since these updrafts coincide with the negative perturbation horizontal wind, upper-layer clouds containing low-density ice particles extend upstream when the perturbation wind speed exceeds the background wind speed. After $t \sim 4$ h, lower-level stratiform orographic clouds transition into cellular-type convective orographic clouds as condensational latent heating enhances local instability, consistent with the cellular organization of orographic convection documented by Kirshbaum and Durran (2004). These convective cells subsequently extend upstream. Occasionally, some convective cells deepen and interact with upper-layer mixed-phase clouds. This interaction leads to intermittent heavy precipitation caused by melting of high-density ice particles or direct precipitation of graupel or hail (Fig. 3d).

Figure 4 shows the Hovmöller diagrams of surface rain rate (shaded) and ice-phase precipitation rate (contoured at 0.01 mm h^{-1}) in CLN, CNT, and PLT. As described earlier, the transiently generated deep convective system is advected downstream, while steady orographic precipitation occurs near the mountain. This pattern corresponds to Regime III in Chu and Lin (2000), characterized by deep convection forming near the mountain and propagating downstream. In CNT and PLT, orographic precipitation extends upstream

after $t \sim 5$ h. In all cases, ice-phase precipitation becomes dominant near and downstream of the mountain peak after $t \sim 6$ h, as the freezing level gradually decreases over time. In this study, we focus on how aerosol number concentration and upslope steepness modulate surface rainfall over the mountainous terrain through interactions between deep convective orographic clouds and upper-level mixed-phase clouds. Here, 'orographic clouds' refer specifically to terrain-induced deep convective systems that develop along the mountain slopes, while upper-level clouds are distinguished by their formation aloft via wave-induced uplift and their role in modulating precipitation rather than initiating it. Therefore, averaged and accumulated variables from $t = 4$ to 6 h are analyzed to avoid the initial period dominated by the transiently developed deep convective system ($t = 0\text{--}4$ h) and the later stage dominated by ice-phase precipitation ($t = 6\text{--}12$ h).

3.2 Aerosol effects on orographic precipitation

Figure 5 shows the averaged mixing ratios of liquid drops, low-density ice particles, and high-density particles, along with wind vectors from $t = 4$ to 6 h in CLN, CNT, and PLT. During this period, lower-level convective orographic clouds develop over the mountain. In the cases with higher aerosol number concentration, a larger number of condensates results in stronger condensational latent heating, which leads

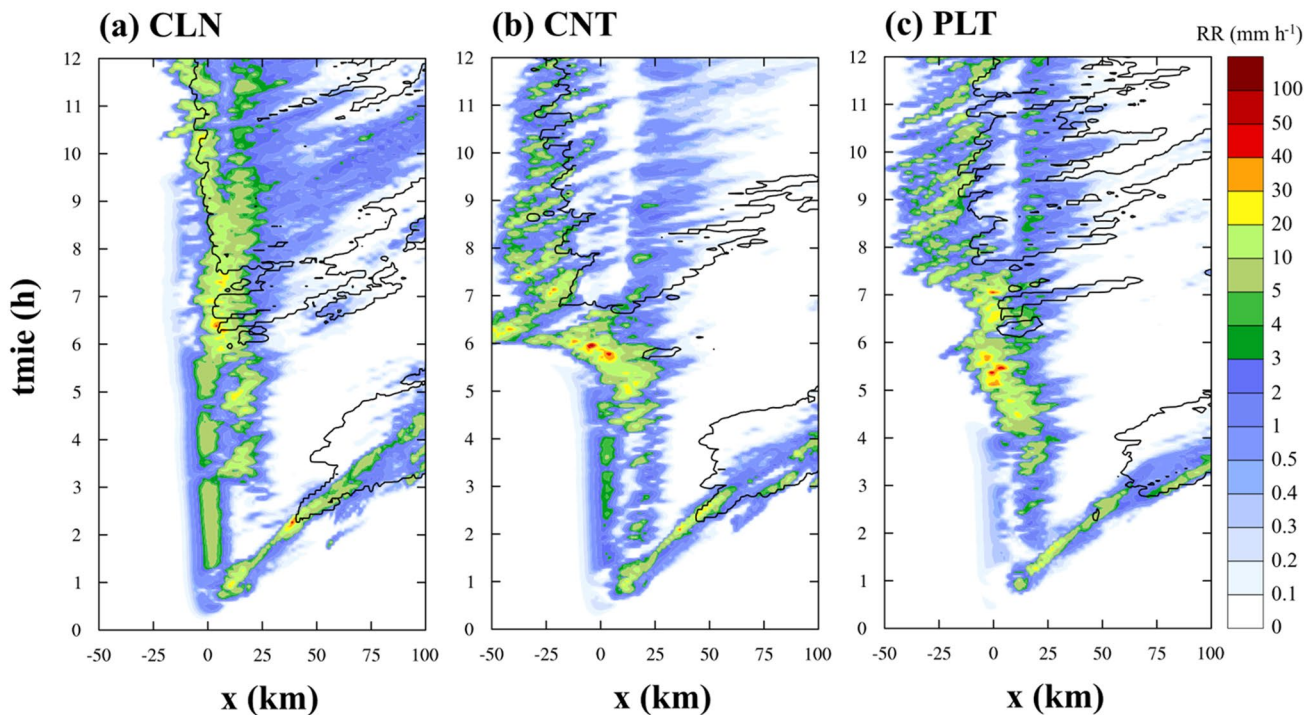


Fig. 4 Hovmöller diagrams of surface rain rate (shaded) and ice-phase precipitation rate (contoured at 0.01 mm h^{-1}) in (a) CLN, (b) CNT, and (c) PLT

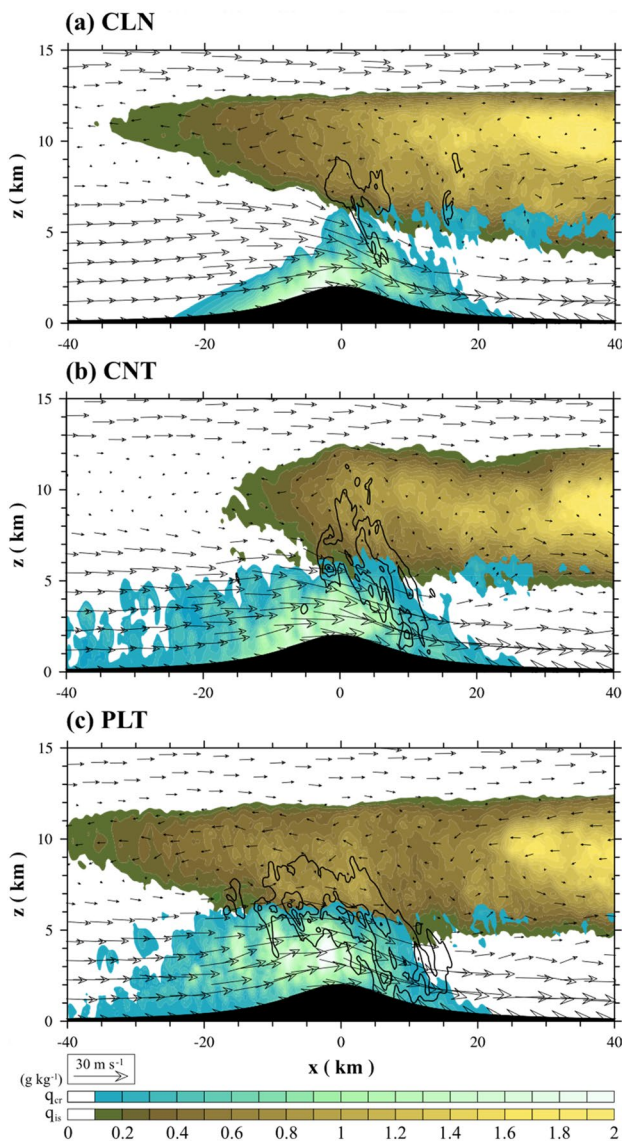


Fig. 5 Same as Fig. 3, but averaged from $t=4$ to 6 h in (a) CLN, (b) CNT, and (c) PLT. The contour interval of high-density ice particle mixing ratio is 0.1 g kg^{-1}

to deeper and stronger convection (Khain et al. 2005; Rosenfeld et al. 2008). As a result, more liquid drops can interact with ice particles in the upper-layer cloud and freeze into ice crystals above the freezing level. These processes increase the mixing ratio of high-density ice particles in the cases with high aerosol number concentration. The high-density ice particles grow via riming in both lower- and upper-layer clouds and enhance surface precipitation through melting or direct sedimentation. This interpretation is consistent with previous findings, including Xiao et al. (2015), who demonstrated that high aerosol number concentrations promote the upward transport of small supercooled liquid droplets, enhancing freezing and riming above the freezing level and

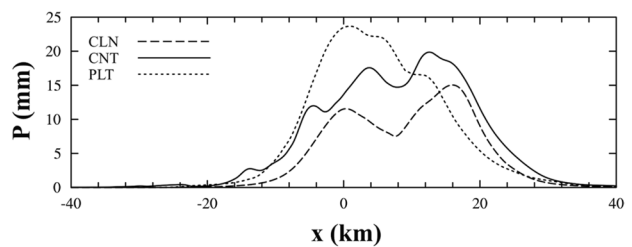


Fig. 6 Accumulated precipitation amount from $t=4$ to 6 h as a function of x in CLN, CNT, and PLT

thereby increasing precipitation efficiency. This mechanism will also be further supported by Fig. 7. These results are also consistent with Munawar et al. (2025), who emphasized the dominant role of CCN in initiating glaciation. Figure 6 and Table 2 show that increasing aerosol number concentration leads to greater total and maximum precipitation amounts and an upstream shift in the location of the maximum precipitation. This dependency of precipitation characteristics on aerosol number concentration is opposite to the shallow, warm orographic precipitation case described in Part I. However, an increase in total and maximum precipitation amounts caused by an increase in aerosol loading has also been reported in previous studies (Khain et al. 2005; Rosenfeld et al. 2008; Xiao et al. 2015; Clavner et al. 2018).

Figure 7 shows the vertical profiles of temperature change due to microphysical processes over the upslope ($x=-50$ – 0 km) and downslope ($x=0$ – 50 km) of the mountain. On both sides, nucleation is strongest in PLT. Over the upslope, the nucleation rate decreases with height, while over the downslope it peaks around 5 km above ground level (AGL) (Fig. 7a and f). A higher number of condensates over the upslope in PLT leads to stronger condensational latent heating there and also stronger evaporative cooling over the downslope, compared to the other cases (Figs. 7b and g). Over the upslope, many liquid drops freeze into ice crystals (Fig. 7d), which then grow through the Wegener-Bergeron-Findeisen (WBF) process in PLT (Figs. 7b and c). This process is followed by intensive riming, which induces strong localized heating over the upslope in PLT (Fig. 7e), where riming is most active across nearly all altitudes. In contrast, riming is relatively suppressed over the downslope in PLT (Fig. 7j). This distribution suggests that the riming zone in PLT has shifted upstream, a feature observed in the case with high aerosol number concentration. Such spatial displacement of the riming zone resembles the mechanism proposed by Chavez and Barros (2023), in which aerosols shift riming activity upwind, extending the hydrometeor growth pathway and enhancing precipitation. In CLN, similar processes, intense freezing and the WBF process, are strongest over the downslope compared to the other cases (Figs. 7g–i). Riming between ice-phase particles and liquid drops primarily

Table 2 Total accumulated surface precipitation amount over 6 h ($t=3$ h to 9 h; P_{tot}), maximum 6-h surface precipitation amount (P_{max}), and the x -location where P_{max} occurs (x_{max}) in the nine simulation cases

a_1 (km)	P_{tot} (mm)			P_{max} (mm)			x_{max} (km)		
	5	10	20	5	10	20	5	10	20
clean	1755	1298	1711	15.8	15.0	33.7	2.0	16.0	3.8
Control	1000	2022	2551	10.6	19.9	29.3	16.0	12.5	-2.0
Polluted	1260	2071	1394	11.8	23.7	25.2	14.0	1.0	4.8

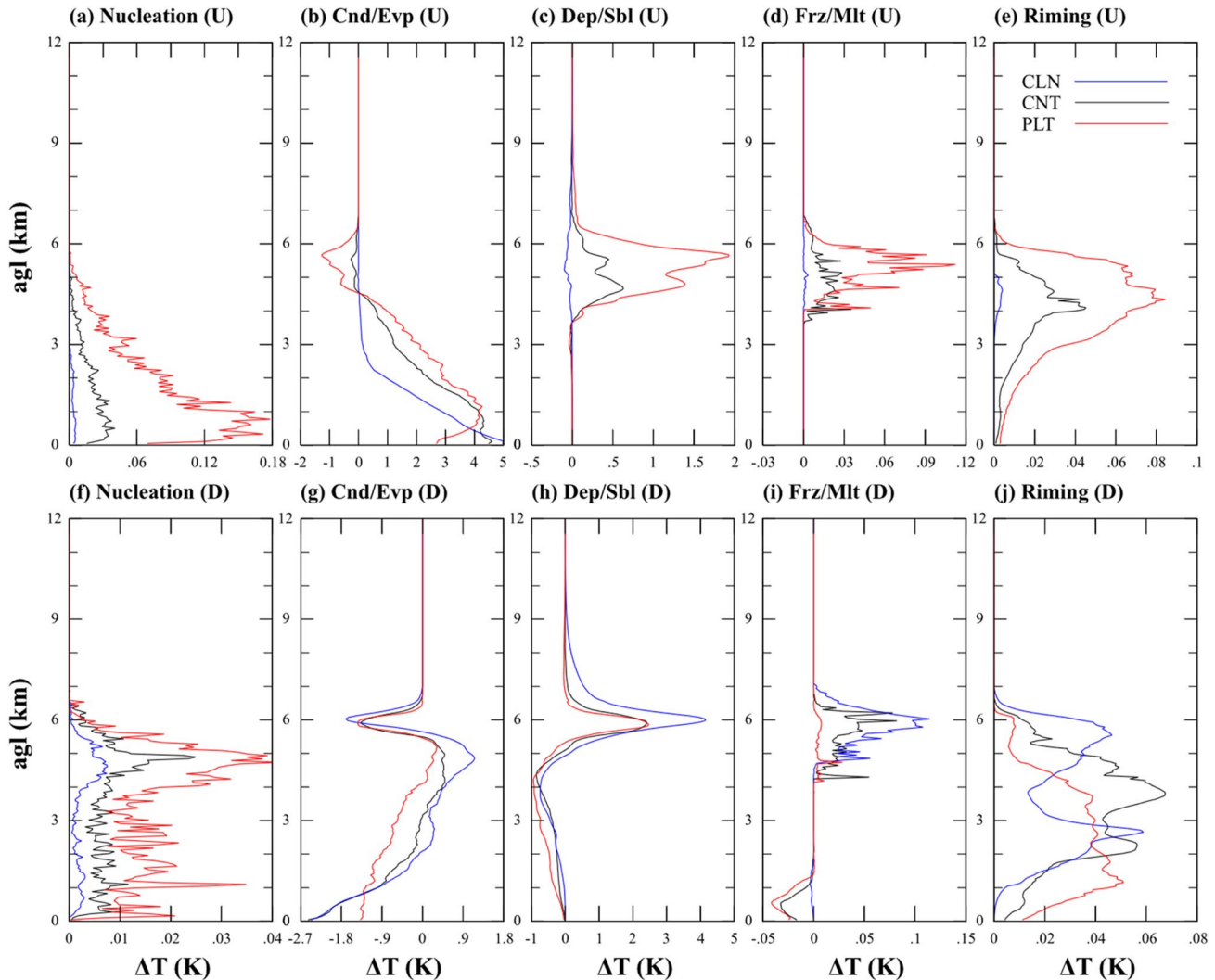


Fig. 7 Vertical profiles of temperature change due to (a, f) nucleation, (b, g) condensation/evaporation, (c, h) deposition/sublimation, (d, i) freezing/melting, and (e, j) riming over the upslope ($x=-50$ –0 km)

(upper panels) and downslope ($x=0$ –50 km) (lower panels) of the mountain in CLN, CNT, and PLT

contributes to enhanced surface precipitation through mixed-phase processes (Figs. 7e and j).

During these processes, the upstream extension of the upper-layer cloud creates an environment that increases the mixing ratio of high-density ice particles via riming when lower-layer convective clouds grow through the freezing level. This environment is associated with advection of ice particles by negative horizontal velocity within mountain

waves over the mountain peak (see Figs. 3 and 5). Figure 8 presents the accumulated advection rates of hydrometeors over the mountain peak ($x=0$) as a function of hydrometeor size and height AGL. The advection rate, defined as the mass flux per logarithmic size interval of hydrometeors, is calculated using the following equation:

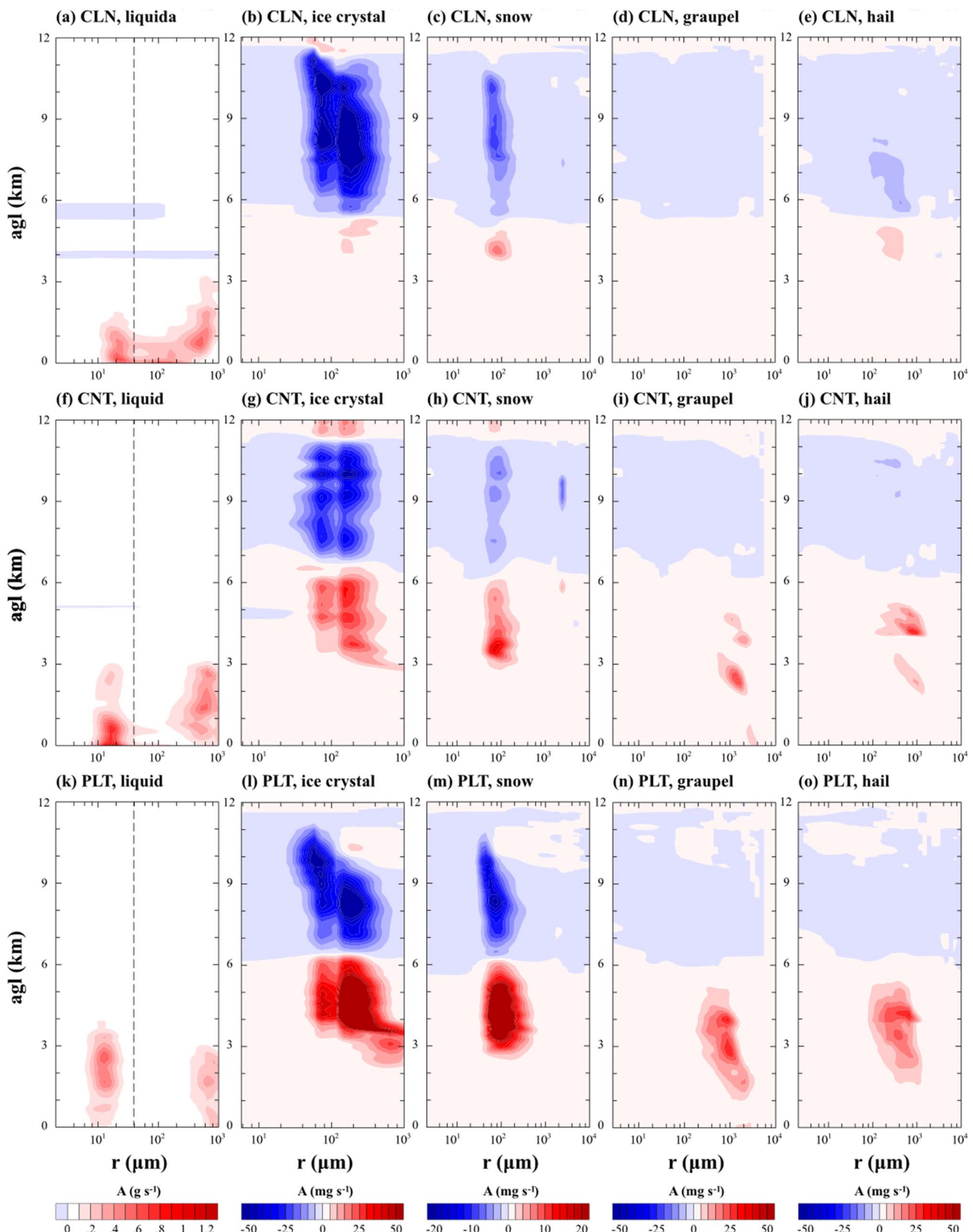


Fig. 8 Accumulated advection rates of (a, f, h) liquid drops, (b, g, l) columnar ice crystals, (c, h, m) snow, (d, i, n) graupel, and (e, j, o) hail across $x=0$ as a function of hydrometeor size and height AGL in

CLN (upper panels), CNT (middle panels), and PLT (lower panels). Dashed lines in (a, f, k) indicate $r=40 \mu\text{m}$, the threshold size separating cloud droplets and raindrops

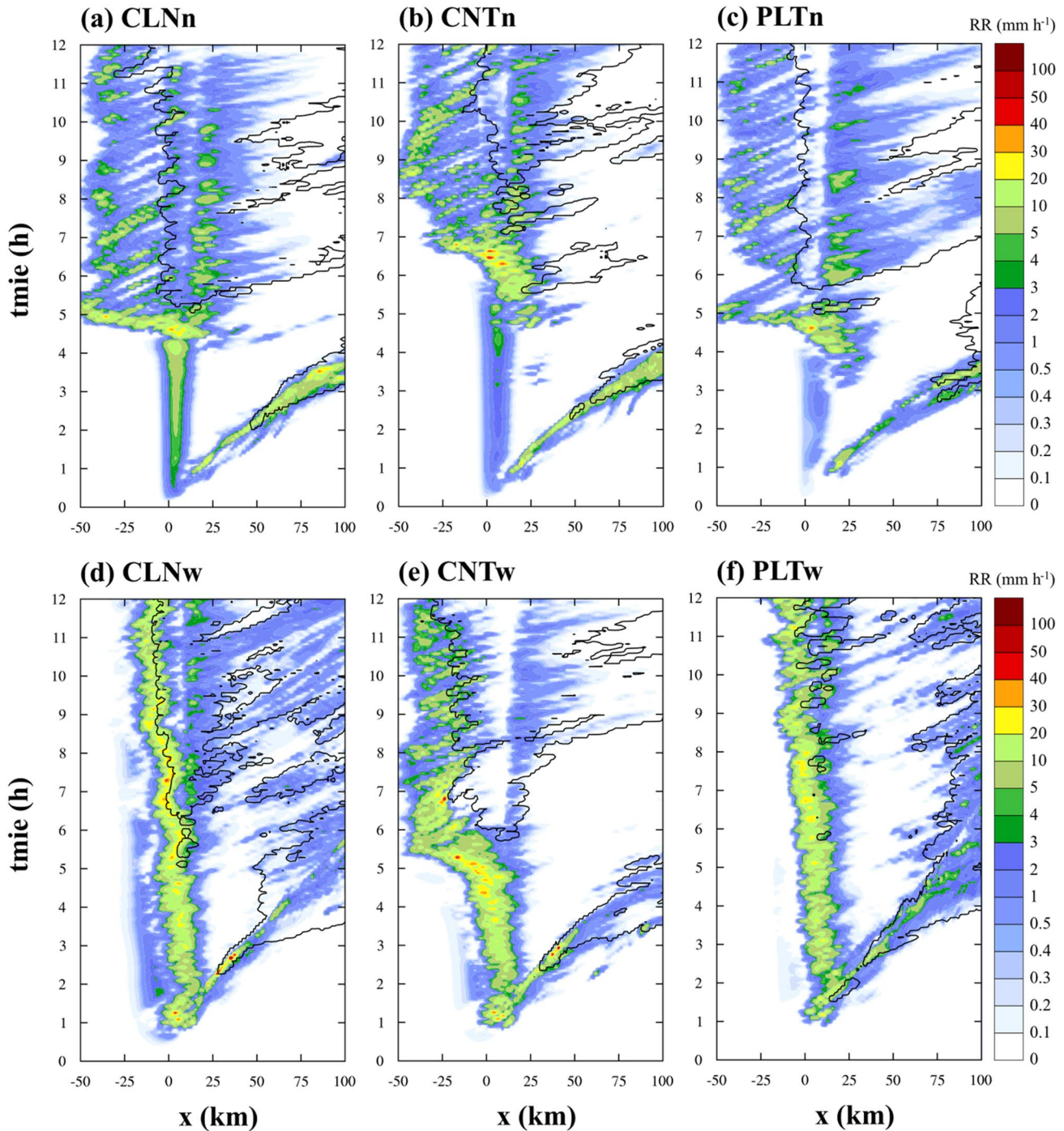


Fig. 9 Same as Fig. 4 except for (a) CLNn, (b) CNTn, (c) PLTn, (d) CLNw, (e) CNTw, and (f) PLTw

$$A(r_H, z) = \rho_H(r_H) u(x = 0, z) q_H(r_H, x = 0, z) / d \ln r_H, \quad (4)$$

where $\rho_H(r_H)$ is the size-dependent density function of each hydrometeor, u is the horizontal velocity, and q_H is the mixing ratio of each hydrometeor.

With higher aerosol number concentration, cloud droplets become smaller, and the advection rate fields suggest the

possible upward extension of lower-layer convective clouds (Fig. 8a, f, and k). The positive advection rate of columnar ice crystals below approximately 6 km AGL is much higher in PLT, while it is nearly absent in CLN (Fig. 8b, g, and l) due to stronger freezing and WBF processes over the upslope in PLT compared to CLN (Figs. 7b–d). Similarly, the negative advection rate in upper layer is larger in

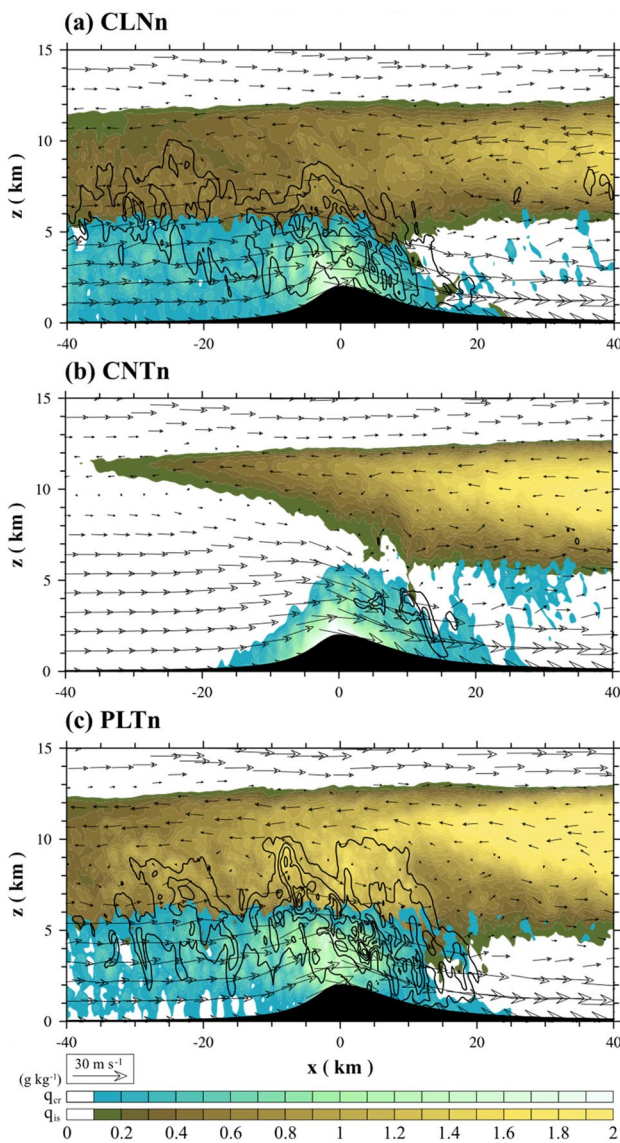


Fig. 10 Same as Fig. 5 except for (a) CLNn, (b) CNTn, and (c) PLTn

CLN than in the other cases. Over the mountain peak, lower-layer convective orographic clouds overlap with upper-layer clouds in PLT (Fig. 5c). In the upper-layer clouds, many ice crystals grow into snow particles, some of which are advected to the upslope side (Fig. 8m). These snow particles further grow through riming in the overlapping layer over the upslope (Fig. 7e), transform into graupel and hail, and are again advected over the mountain peak (Figs. 8n and o). These graupel and hail particles melt and contribute to surface precipitation (Fig. 7i). In CLN, however, the overlap between lower and upper clouds is limited to a narrow region over the mountain peak (Fig. 5a). Although many ice particles generated and grown over the downslope are advected over the mountain peak, their further growth is limited. Moreover, even though riming is active, ice particles

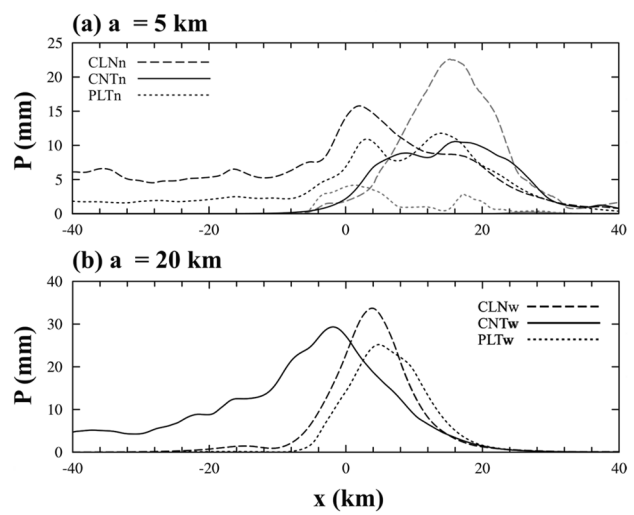


Fig. 11 Accumulated liquid (black) and ice (gray) precipitation amounts from $t=4$ to 6 h as a function of x in the cases with (a) $a_1=5 \text{ km}$ and (b) 20 km

in CLN often fail to reach the surface over the downslope (Fig. 7j). For this reason, the total and maximum precipitation amounts in CLN are lower than those in the other cases.

The upstream extension of the upper-level ice-phase clouds observed in CNT and PLT may be explained by a combination of wave-induced ascent and nonlinear convective dynamics. Initially, mountain waves generate upper-tropospheric ascent that supports ice cloud formation on the lee side. In addition, Han and Baik (2012) demonstrated that under strongly nonlinear conditions, deep convection can induce flow reversal near the upper upwind edge of the main updraft, manifested as overturning streamlines above the convective core. This flow is characterized by downstream flow just above the convection and upstream flow farther aloft, forming a rotor-like, closed-loop structure. Such reversed flow can lift and advect ice particles formed near the convective top upslope, facilitating the upstream extension of upper-level clouds. This mechanism is consistent with the wave-induced critical-level duct and flow reversal structures described in Clark and Peltier (1984). Our simulations exhibit signatures of such behavior (e.g., Figs. 8g and l), where opposing ice advection patterns above and below $\sim 6 \text{ km}$ coincide with elevated ice water content and localized overturning motion. These features suggest a plausible pathway for upstream broadening and vertical interaction between upper- and lower-level cloud layers.

3.3 Modulation of aerosol effects on orographic precipitation by upslope steepness

In Part I, the sensitivity of aerosol effects on orographic precipitation to upslope steepness was examined. As discussed

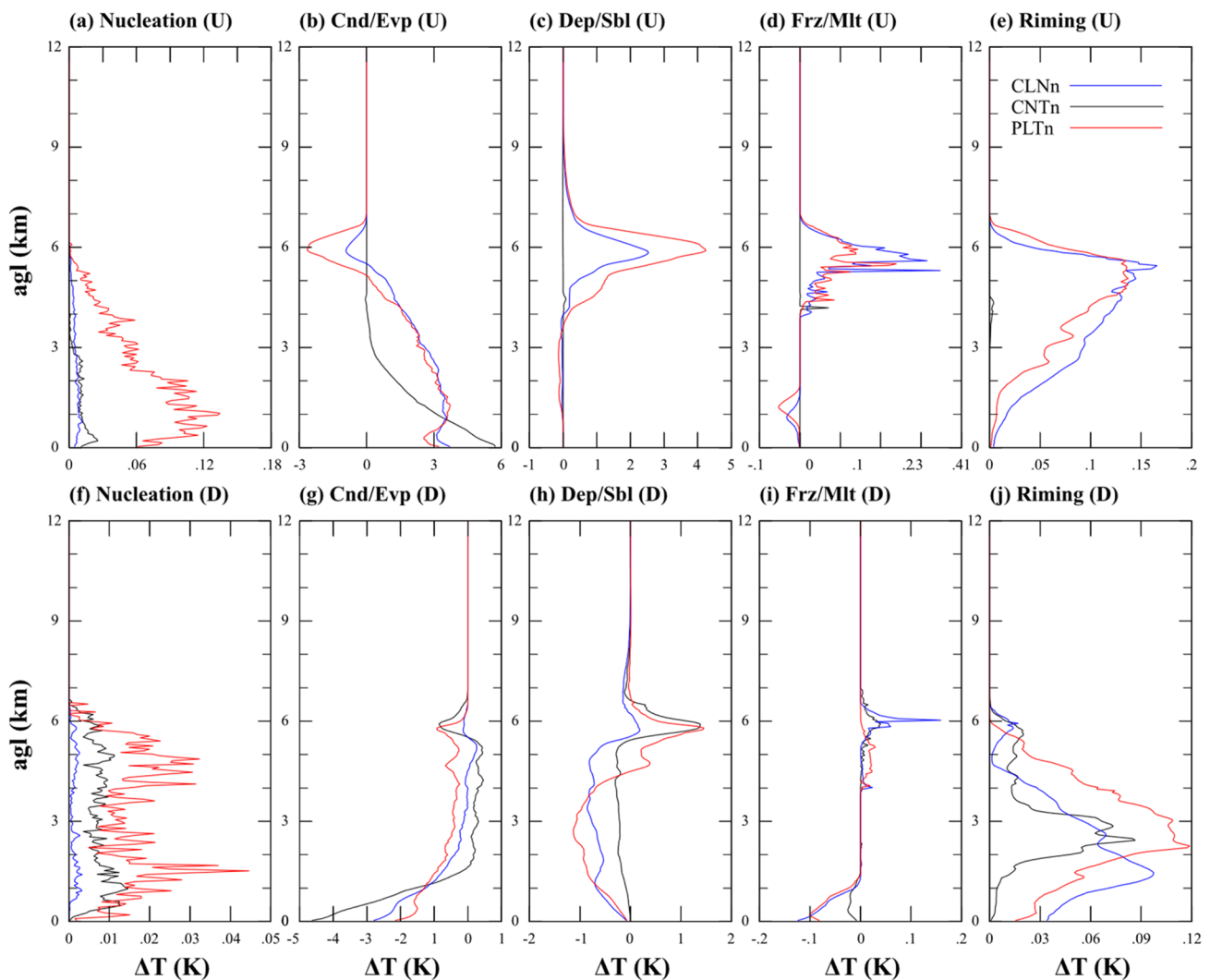


Fig. 12 Same as Fig. 7 except for the cases with $a_1=5$ km

in Part I, Fig. 9 shows that the decrease in precipitation amount and the downstream shift of the location of the maximum precipitation are clear in the cases with $a_1=5$ km (Figs. 9a–c) and less apparent in the cases with $a_1=20$ km (Figs. 9d–f) during the early stage ($t=0\text{--}4$ h). As time progresses, however, the sensitivity evolves differently depending on the case. In the cases with $a_1=5$ km, the upstream extension of the precipitation area starts earlier in PLTn and CLNn than in CNTn. This results in lighter total and maximum precipitation in CNTn compared to the other cases (Table 2). In the cases with $a_1=20$ km, a broad precipitation region over the mountain is present in all cases. In CLNw and PLTw, however, the upstream extension of precipitation area does not occur. This results in heavier total precipitation in CNTw compared to the other cases (Table 2). These comparisons collectively reveal a non-monotonic relationship

between aerosol number concentration and precipitation characteristics under varying upslope steepness, a pattern also identified in previous studies (e.g., Xiao et al. 2015; Chen et al. 2025). Such non-monotonicity underscores the complex interactions between orographic dynamics, latent heating of convective clouds, and microphysical processes.

Figure 10 shows the averaged mixing ratio of liquid drops, low-density ice particles, and high-density ice particles and wind vectors from $t=4$ to 6 h in CLNn, CNTn, and PLTn. In CNTn, narrower lower-layer orographic clouds are generated over the upslope due to the narrower upslope width. Although high-density ice particles affect precipitation over the downslope, the interaction between lower- and upper-layer clouds is weaker compared to the other cases. Surface precipitation is concentrated over the downslope, and precipitation over the upslope is very limited (solid

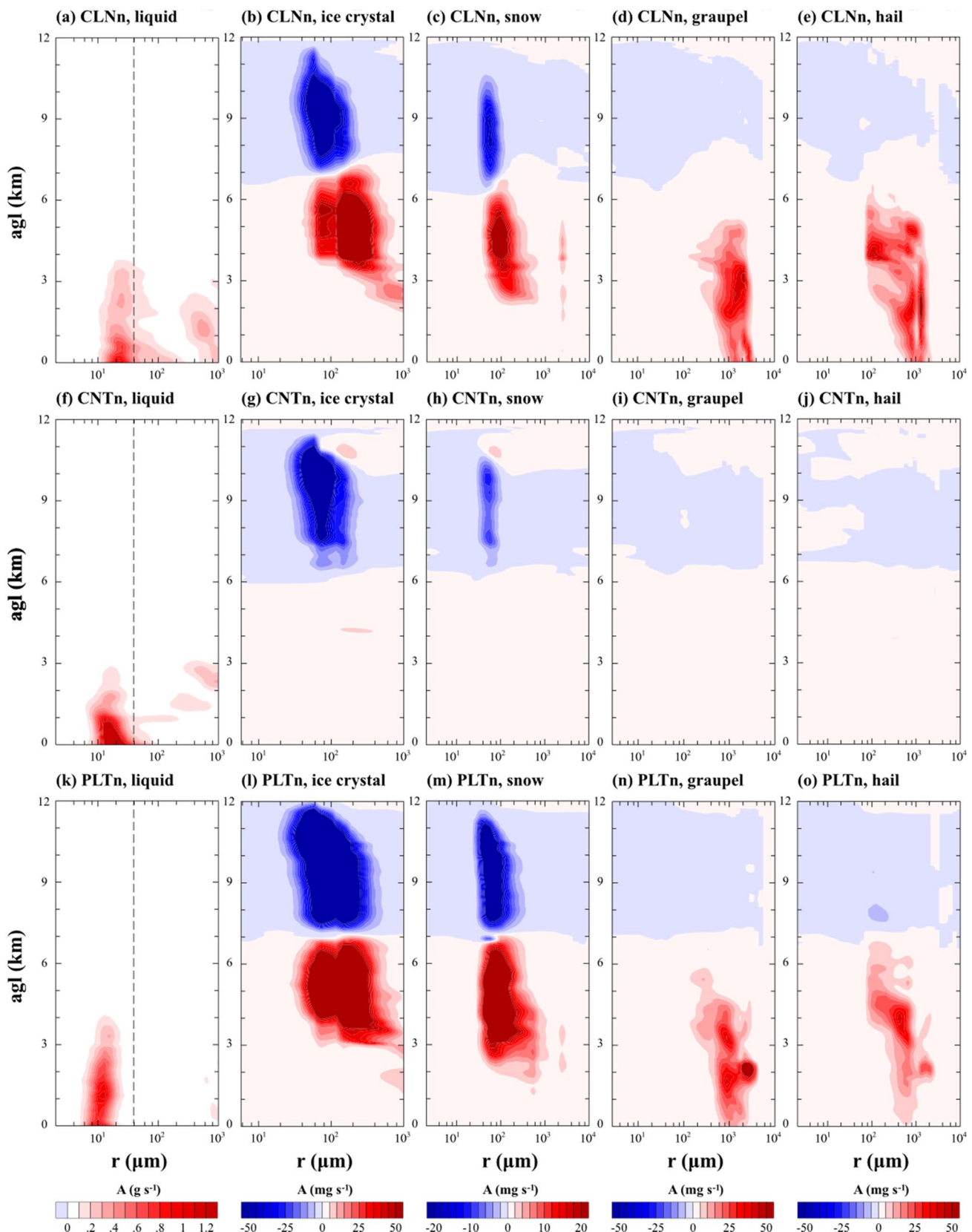


Fig. 13 Same as Fig. 8 except for the cases with $a_1=5 \text{ km}$

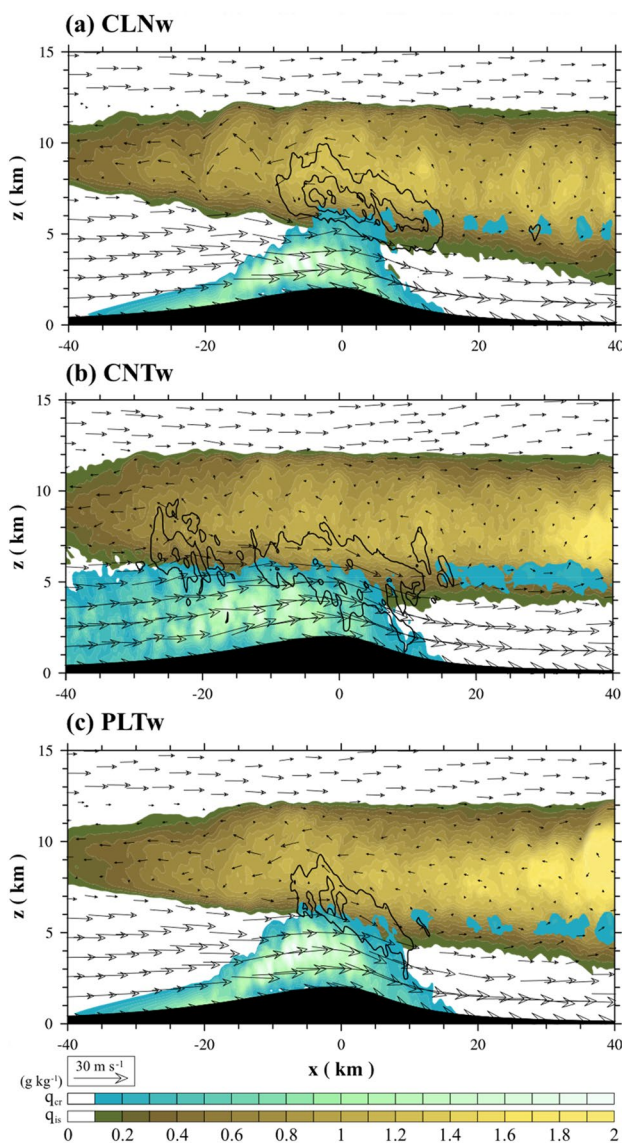


Fig. 14 Same as Fig. 5 except for (a) CLNw, (b) CNTw, and (c) PLTw

line of Fig. 11a). In CLNn and PLTn, upper-layer clouds extend upstream, which clearly contributes to increased precipitation over the upslope. This upstream extension of upper-layer cloud also appears to facilitate the development of lower-layer clouds, which is more distinct in these cases compared to CNTn (Fig. 10). Among all cases, CLNn exhibits the strongest ice-phase precipitation, reflecting favorable upper-layer cloud interactions and enhanced mixed-phase processes.

Over both the upslope and downslope, nucleation is strongest in PLTn (Figs. 12a and 12f). As discussed in Part I, in these cases, nucleated cloud droplets do not grow sufficiently before reaching the mountain peak due to the short advection time scale over the upslope, even though the steep

upslope generates strong convection. For this reason, cloud droplets with relatively small radii appear more widely distributed and persist lower and middle layers in asymmetric mountain cases (compare Fig. 8a, f, and k and Fig. 13a, 13f, and 13k). This is supported by the broader and stronger horizontal advection rates of small droplets, which indicate their presence at higher altitudes and suggest that lower-layer convection extends to those levels, although advection rates do not directly represent mass. In the cases with higher aerosol number concentration, strong condensational latent heating produces deeper convective clouds over the upslope and many small liquid drops are frozen above the freezing level (Figs. 12b and d). Compared to the other cases, the WBF process is strongest in PLTn (Fig. 12b and c). Similar to PLT, frozen and grown ice particles continue to grow via strong riming over both the upslope and downslope, resulting in heavy surface precipitation through melting or direct sedimentation of ice-phase particles (Figs. 11a, 12e, j, and 13k–o).

In CLNn, lower-layer clouds containing liquid drops develop through the freezing level. The advection pattern of liquid drops in Fig. 13a suggests active droplet growth, and Fig. 13b shows that ice particle advection is centered at relatively large sizes. As a result, the sizes of high-density ice particles become very large, contributing to heavy liquid- and ice-phase precipitation (Figs. 11a, 13d, e). In CNTn, the condensational latent heating is weaker than in PLTn (Fig. 12a), and the cloud droplet advection pattern (Fig. 13a and f) shows narrower size distribution and shallower vertical extent in CNTn than in CLNn, suggesting slower droplet growth. As a result, the interaction between lower- and upper-layer clouds is inhibited over the upslope (Figs. 12b–e). However, advected liquid drops that pass over the mountain peak continue to grow and freeze over the downslope, and the resulting ice crystals are further enhanced via the WBF process and riming (Figs. 12g–j). Consequently, precipitation in CNTn is concentrated over the downslope (Fig. 11a).

Figure 14 shows the averaged mixing ratios of the liquid drops, low-density ice particles, and high-density ice particles, along with wind vectors from $t=4$ to 6 h in CLNw, CNTw, and PLTw. Over the wide upslope, broader but weaker convective orographic clouds form, compared to the cases with the symmetric mountain and narrow upslope. In CLNw and PLTw, lower- and upper-layer clouds interact only near the mountain peak (Fig. 14a and c). In CNTw, however, the interaction over the upslope occurs due to the upstream extension of lower-layer clouds (Fig. 14b). For this reason, the total precipitation amount in CNTw is larger than in CLNw and PLTw (Table 2). Surface precipitation is concentrated over the downslope in CLNw and PLTw and is smaller in PLTw than CLNw (Table 2 and Fig. 11b).

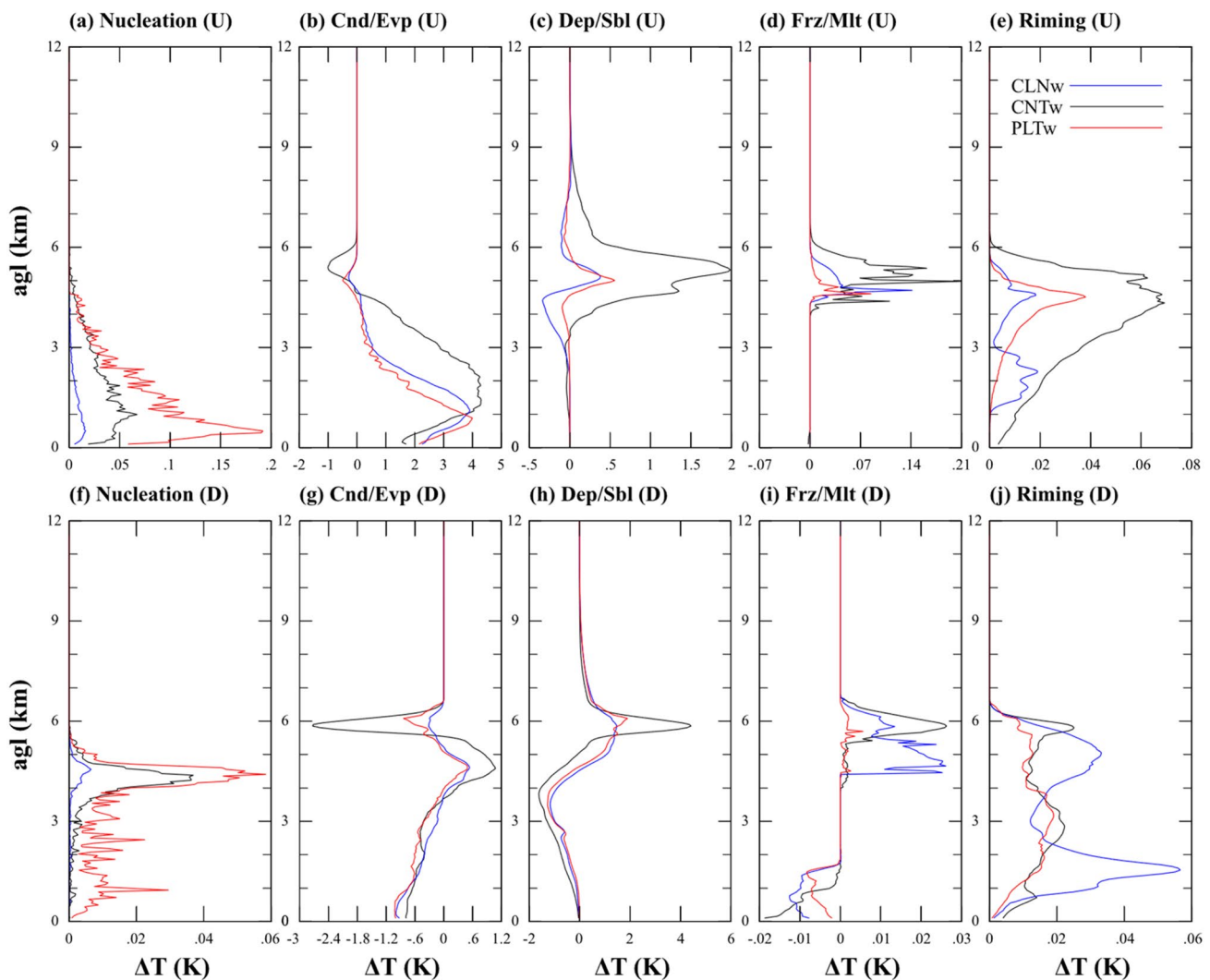


Fig. 15 Same as Fig. 7 except for the cases with $a_1=20$ km

As discussed in Part I, cloud droplets over the wide upslope grow sufficiently into raindrops. The broader and stronger advection of larger droplets near the mountain peak (Fig. 16a, f, and k) implies that many cloud droplets may have already grown into raindrops before reaching the mountain peak. Similar to the other cases, the nucleation rate is highest in PLTw over both the upslope and downslope (Figs. 15a and f). In CNTw, many ice crystals are generated from frozen droplets and grow into snow particles via the WBF process at approximately 6 km AGL over the downslope (Figs. 15g–i). These low-density ice particles are advected toward the upslope side (Figs. 16g and h). In addition, the freezing-induced heating is strongest in CNTw (Fig. 15d). Low-density ice

particles generated over the upslope and advected from the downslope continue to grow into high-density ice particles through deposition and riming and are again advected downslope side (Figs. 15b–e and 16g–j). The melted high-density ice particles enhance surface precipitation via melting. In CLNw and PLTw, however, such mixed-phase processes are inhibited. In CLNw, the narrower and weaker advection of cloud droplets in Fig. 16a is consistent with faster drop growth, which reduces the remaining droplet population above the freezing level. In PLTw, the limited vertical and size extent of droplet advection in Fig. 16k suggests weak convective development, making it difficult for small liquid particles to grow into large ice particles.

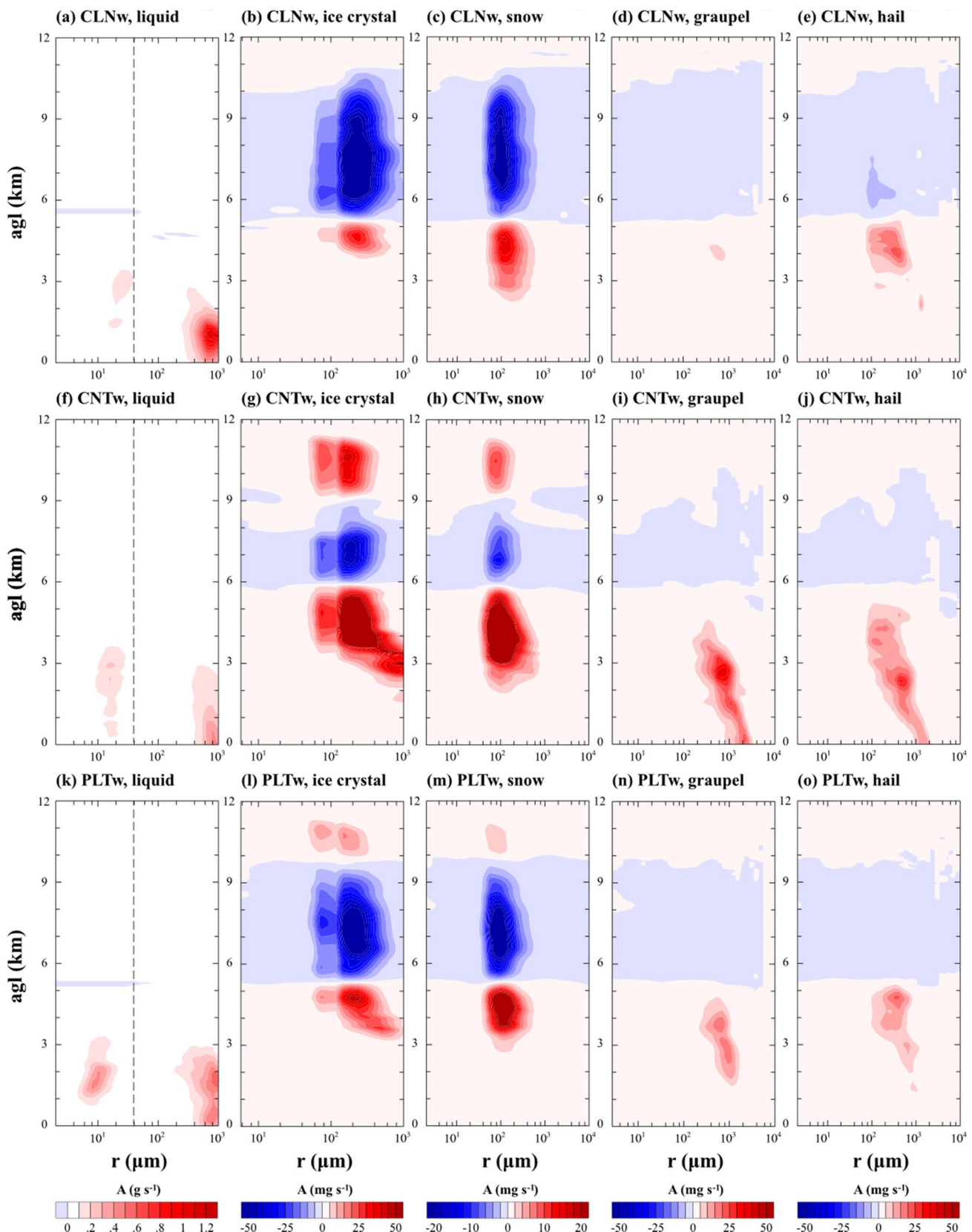


Fig. 16 Same as Fig. 8 except for the cases with $a_1 = 20 \text{ km}$

4 Summary and conclusions

In this study, the sensitivity of aerosol effects on orographic precipitation from deep convective clouds to windward slope steepness is examined using the WRF model coupled with a bin microphysics scheme. Aerosol number concentration and the windward half-width of a bell-shaped mountain are systematically controlled to construct nine simulation cases.

During the early stage, orographic precipitation near the mountain is primarily produced by lower-layer clouds. At this stage, the dependencies on aerosol number concentration and upslope steepness resemble those of warm, shallow orographic convection discussed in Part I. As time progresses, however, lower-layer convective clouds vigorously develop and upper-layer mixed-phase clouds extend upstream in some cases. When both strong convection and sufficient vertical cloud overlap occur, the interaction between lower- and upper-layer clouds leads to enhanced surface precipitation via melting or direct sedimentation of high-density ice particles, such as graupel and hail.

In the symmetric mountain cases, increasing aerosol number concentration leads to stronger convection and more active mixed-phase microphysical processes (freezing, the WBF process, and riming), resulting in greater total and maximum precipitation amounts. However, under steep and gentle upslope conditions, the trends are non-monotonic. In CLNn, strong convective clouds induced by the steep upslope and the rapid growth of liquid drops and ice particles lead to intense precipitation. In PLTn, although drop growth is slower, strong condensational latent heating compensates for it and produces heavy precipitation. In contrast, in CNTn, both the development of convection and mixed-phase processes are suppressed, resulting in weaker precipitation.

In the wide upslope cases, CNTw exhibits enhanced precipitation even with the weak orographic forcing, due to condensational heating that supports vertical cloud development through the freezing level. In CLNw, the low aerosol number concentration limits the formation of cloud droplets which act as the primary source of ice crystals above the freezing level. As a result, the interaction between cloud layers and subsequent precipitation is suppressed. In PLTw, the interaction is also suppressed. This is not due to a lack of condensates, but because the gentle upslope induces weak orographic uplift, limiting the development of convection despite strong aerosol-induced heating.

This study adopts a stably stratified atmosphere with high CAPE to allow deep convection to develop and to facilitate controlled orographic cloud formation via forced uplift across a bell-shaped mountain. Without sufficient CAPE, down-drafts associated with mountain waves would likely suppress

convection. The use of a two-dimensional mountain configuration allows for clear and systematic interpretations of the aerosol–cloud–precipitation interactions by minimizing the complexity associated with fully three-dimensional flow structures. However, this simplified setting may not capture features such as lateral cloud spreading or along-ridge variability that are relevant in real terrain. The results demonstrate that lower-layer cloud development through the freezing level is a key prerequisite for activating mixed-phase interactions and achieving strong surface precipitation. Therefore, vertical instability, in addition to aerosol number concentration and mountain geometry, plays a crucial role in modulating orographic precipitation. Future studies should explore how different vertical soundings and terrain geometries, including three-dimensional mountain shapes, influence aerosol–cloud–precipitation interactions under various terrain settings.

Acknowledgements The authors thank two anonymous reviewers for providing helpful comments and suggestions. This second author was supported by the National Research Foundation of Korea (NRF) under grant RS-2025-00562044. The authors thank supercomputer management division of the Korea Meteorological Administration for providing us with the supercomputer resource.

Author contributions J.-J. Baik designed the numerical experiments. J. M. Seo performed the simulations, analyzed the results, and prepared the main manuscript. Both authors contributed to the interpretation of the results and the revision of the manuscript.

Funding National Research Foundation of Korea, RS-2025-00562044.

Data availability No datasets were generated or analysed during the current study.

Declarations

Conflict of interest The authors declare no conflict of interests.

Open Access This article is licensed under a Creative Commons Attribution 4.0 International License, which permits use, sharing, adaptation, distribution and reproduction in any medium or format, as long as you give appropriate credit to the original author(s) and the source, provide a link to the Creative Commons licence, and indicate if changes were made. The images or other third party material in this article are included in the article's Creative Commons licence, unless indicated otherwise in a credit line to the material. If material is not included in the article's Creative Commons licence and your intended use is not permitted by statutory regulation or exceeds the permitted use, you will need to obtain permission directly from the copyright holder. To view a copy of this licence, visit <http://creativecommons.org/licenses/by/4.0/>.

References

- Chavez SP, Barros AP (2023) Aerosol indirect effects on orographic clouds and precipitation. *Front Earth Sci* 11:1025266
- Chen S-H, Lin Y-L (2005) Orographic effects on a conditionally unstable flow over an idealized three-dimensional mesoscale mountain. *Meteorol Atmos Phys* 88:1–21
- Chen S-H, Lin Y-L, Zhao Z (2008) Effects of unsaturated moist Froude number and orographic aspect ratio on a conditionally

- unstable flow over a mesoscale mountain. *J Meteorol Soc Jap* 86:353–367
- Chen F, Yang Y, Yu L, Li Y, Liu W, Liu Y, Lolli S (2025) Distinct effects of fine and coarse aerosols on microphysical processes of shallow-precipitation systems in summer over southern China. *Atmos Chem Phys* 25:1587–1601
- Cheng CT, Wang WC, Chen JP (2007) A modelling study of aerosol impacts on cloud microphysics and radiative properties. *Quart J Roy Meteorol Soc* 133:283–297
- Chu C-M, Lin Y-L (2000) Effects of orography on the generation and propagation of mesoscale convective systems in a two-dimensional conditionally unstable flow. *J Atmos Sci* 57:3817–3837
- Clark TL, Peltier WR (1984) Critical level reflection and the resonant growth of nonlinear mountain waves. *J Atmos Sci* 41:3122–3134
- Clavner M, Cotton WR, van den Heever SC, Saleeby SM, Pierce JR (2018) The response of a simulated mesoscale convective system to increased aerosol pollution: Part I: Precipitation intensity, distribution, and efficiency. *Atmos Res* 199:193–208
- Colle BA (2004) Sensitivity of orographic precipitation to changing ambient conditions and terrain geometries: an idealized modeling perspective. *J Atmos Sci* 61:588–606
- Durran DR (1990) Mountain waves and downslope winds. *Meteorol Monogr* 23:59–81
- Fan JW, Leung LR, Li ZQ, Morrison H, Chen HB, Zhou YQ, Qian Y, Wang Y (2012) Aerosol impacts on clouds and precipitation in eastern China: Results from bin and bulk microphysics. *J Geophys Res* 117:D00K36
- Fan JW, Wang Y, Rosenfeld D, Liu X (2016) Review of aerosol-cloud interactions: Mechanisms, significance, and challenges. *J Atmos Sci* 73:4221–4252
- Givati A, Rosenfeld D (2004) Quantifying precipitation suppression due to air pollution. *J Appl Meteor Climatol* 43:1038–1056
- Guo J, Deng M, Fan J, Li Z, Chen Q, Zhai P, Dai Z, Li X (2014) Precipitation and air pollution at mountain and plain stations in northern China: Insights gained from observations and modeling. *J Geophys Res Atmos* 119:4793–4807
- Han J-Y, Baik J-J (2012) Nonlinear effects on convectively forced two-dimensional mesoscale flows. *J Atmos Sci* 69:3391–3404
- Jirak IL, Cotton WR, Woodley WL (2006) Effect of air pollution on precipitation along the front range of the rocky mountains. *J Appl Meteor Climatol* 45:236–245
- Khain A (2009) Notes on state-of-the-art investigations of aerosol effects on precipitation: a critical review. *Environ Res Lett* 4:015004
- Khain A, Sednev I (1996) Simulation of precipitation formation in the Eastern Mediterranean coastal zone using a spectral microphysics cloud ensemble model. *Atmos Res* 43:77–110
- Khain AP, Ovtchinnikov M, Pinsky M, Pokrovsky A, Krugliak H (2000) Notes on the state-of-the-art numerical modeling of cloud microphysics. *Atmos Res* 55:159–224
- Khain AP, Pokrovsky A, Pinsky M, Seifert A, Phillips V (2004) Simulation of effects of atmospheric aerosols on deep turbulent convective clouds using a spectral microphysics mixed-phase cumulus cloud model. Part I: model description and possible applications. *J Atmos Sci* 61:2963–2982
- Khain A, Rosenfeld D, Pokrovsky A (2005) Aerosol impact on the dynamics and microphysics of deep convective clouds. *Quart J Roy Meteorol Soc* 131:2639–2663
- Khain A, Rosenfeld D, Pokrovsky A, Blahak U, Ryzhkov A (2011) The role of CCN in precipitation and hail in a mid-latitude storm as seen in simulations using a spectral (bin) microphysics model in a 2D dynamic frame. *Atmos Res* 99:129–146
- Kirshbaum DJ, Durran DR (2004) Factors governing cellular convection in orographic precipitation. *J Atmos Sci* 61:682–698
- Lee H, Baik J-J (2016) Effects of turbulence-induced collision enhancement on heavy precipitation: the 21 September 2010 case over the Korean Peninsula. *J Geophys Res Atmos* 121:12319–12342
- Lynn BH, Khain A, Dudhia J, Rosenfeld D, Pokrovsky A, Seifert A (2005a) Spectral (bin) microphysics coupled with a mesoscale model (MM5). Part I: Model description and first results. *Mon Wea Rev* 133:44–58
- Lynn BH, Khain A, Dudhia J, Rosenfeld D, Pokrovsky A, Seifert A (2005b) Spectral (bin) microphysics coupled with a mesoscale model (MM5). Part II: simulation of a CaPE rain event with a squall line. *Mon Wea Rev* 133:59–71
- Lynn B, Khain A, Rosenfeld D, Woodley WL (2007) Effects of aerosols on precipitation from orographic clouds. *J Geophys Res* 112:D10225
- Miglietta MM, Rotunno R (2009) Numerical simulations of conditionally unstable flows over a mountain ridge. *J Atmos Sci* 66:1865–1885
- Munawar I, Zhu Y, Wang M, Rosenfeld D, Liu J, Wang Y (2025) The dominant role of aerosol's CCN effect in cloud glaciation. *Npj Clim Atmos Sci* 8:121
- Pathirana A, Herath S, Yamada T (2005) Simulating orographic rainfall with a limited-area, non-hydrostatic atmospheric model under idealized forcing. *Atmos Chem Phys* 5:215–226
- Roe GH, Baker MB (2006) Microphysical and geometrical controls on the pattern of orographic precipitation. *J Atmos Sci* 63:861–880
- Rosenfeld D, Givati A (2006) Evidence of orographic precipitation suppression by air pollution-induced aerosols in the western United States. *J Appl Meteor Climatol* 45:893–911
- Rosenfeld D, Dai J, Yu X, Yao Z, Xu X, Yang X, Du C (2007) Inverse relationship between amounts of air pollution and orographic precipitation. *Science* 315:1396–1398
- Rosenfeld D, Lohmann U, Raga GB, O'Dowd CD, Kulmala M, Fuzzi S, Reissell A, Andreae MO (2008) Flood or drought: How do aerosols affect precipitation? *Science* 321:1309–1313
- Seo JM, Lee H, Moon S, Baik J-J (2020) How mountain geometry affects aerosol-cloud-precipitation interactions: Part I. Shallow convective clouds. *J Meteorol Soc Jap* 98:43–60
- Sever G, Lin Y-L (2017) Dynamical and physical processes associated with orographic precipitation in a conditionally unstable uniform flow: variation in basic-state wind speed. *J Atmos Sci* 74:449–466
- Skamarock, W. C., J. B. Klemp, J. Dudhia, D. O. Gill, D. M. Barker, M. G. Duda, X. Huang, W. Wang, and J. G. Powers, 2008: A description of the advanced research WRF version 3. NCAR Tech Note, NCAR/TN-475+STR, 8 pp., Natl. Cent. for Atmos. Res., Boulder, Colo.
- Smith RB (1979) The influence of mountains on the atmosphere. *Adv Geophys* 21:87–230
- Tao W-K, Chen J-P, Li Z, Wang C, Zhang C (2012) Impact of aerosols on convective clouds and precipitation. *Rev Geophys* 50:RG2001
- Weisman MM, Klemp JB (1982) The dependence of numerically simulated convective storms on vertical wind shear and buoyancy. *Mon Wea Rev* 110:504–520
- Xiao H, Yin Y, Jin L, Chen Q, Chen J (2014) Simulation of aerosol effects on orographic clouds and precipitation using WRF model with a detailed bin microphysics scheme. *Atmos Sci Lett* 15:134–139
- Xiao H, Yin Y, Jin L, Chen Q, Chen J (2015) Simulation of the effects of aerosol on mixed-phase orographic clouds using the WRF model with a detailed bin microphysics scheme. *J Geophys Res Atmos* 120:8345–8358

- Xue H, Feingold G (2006) Large-eddy simulations of trade wind cumuli: Investigation of aerosol indirect effects. *J Atmos Sci* 63:1605–1622
- Xue L, Teller A, Rasmussen R, Geresdi I, Pan Z (2010) Effects of aerosol solubility and regeneration on warm-phase orographic clouds and precipitation simulated by a detailed bin microphysical scheme. *J Atmos Sci* 67:3336–3354

Publisher's Note Springer Nature remains neutral with regard to jurisdictional claims in published maps and institutional affiliations.